Near-tip closure and cyclic plasticity in Ni-based single crystals

S. Rabbolini [a,*], P.G. Luccarelli [a], S. Beretta [a], S. Foletti [a], H. Sehitoglu [b]

[a] Department of Mechanical Engineering, Politecnico di Milano, Via La Masa 1, 20156 Milan, Italy
[b] Department of Mechanical Science and Engineering, University of Illinois at Urbana-Champaign, 1206 W Green Street, 61801 Urbana, IL, USA

ARTICLE INFO

ABSTRACT

Fatigue crack growth was investigated in a $[0\,0\,1]$ oriented single crystal specimen, made of a Ni-based superalloy, Haynes 230. Crack propagation was characterized with digital image correlation: crack closure, measured by analyzing the relative displacements of crack flanks, showed closure levels much lower than polycrystal alloys. Reversed plastic zones were calculated from regressed stress intensity factor ranges and compared to the strain field measured at the crack tip. Experimental results were compared to those provided by a numerical model, which considered both crack propagation and single crystal anisotropic behavior, in terms of crack opening levels and crack tip cyclic plastic zones. Results of the numerical simulations were in good agreement with the experiments.

© 2016 Elsevier Ltd. All rights reserved.

1. Introduction

The continuously increasing demand for sustainable and efficient energy has led to the development of innovative alloys, capable of working in very aggressive conditions, such as highly corrosive environments at high temperature. Recently, the energy and aerospace industries have shown a renewed interest in Nickel based superalloys, since they exhibit an improved resistance to creep, corrosion and oxidation, properties that make them the favorite candidate for components such as turbine blades and combustors [1].

A further improvement on material properties can be obtained working on the microstructure of the alloy: an enhanced creep resistance, for example, can be obtained adopting single crystal components, since a single crystal structure does not include polycrystalline grain boundaries, the location in which voids, the features responsible for creep failure, nucleate and grow. On the other hand, single crystal components require the development of advanced design techniques, because they exhibit a marked anisotropic behavior, which is an important factor even in crack propagation, since it has been shown that crack propagation occurs in planes related to crystal slip systems orientation [2]. Accordingly, an accurate description of crack propagation in single crystals is possible only together with an appropriate crystal plasticity model.

In the literature, different crystal plasticity codes have been proposed, with the main aim to describe crack nucleation in polycrystalline aggregates [3]. The formulation of crystal plasticity is due to the works of Taylor, Rice, Hill, Asaro and Needleman [4–7]: starting from experimental observations, in these models, inelastic strain is computed as a function of slip occurring in particular crystallographic planes. An initial application of crystal plasticity to the study of the plastic zone in a single crystal was presented in [8]. Another application of crystal plasticity to the study of the crack tip field can be found in [9], in which the simulation of a cracked C(T) specimen is performed. A comparison between numerical and analytical results of crack tip fields in single crystal is reported in [10]. All these studies were performed considering a single load ramp. An application of crystal plasticity to the study of fatigue can be found in [11], in which crack opening loads were studied in a polycrystalline aggregate. The same approach was employed by Potirniche et al. [12] to study short crack propagation in aluminum. Recently, a different approach based on cohesive elements has been proposed in the literature [13].

1.1. Scope: crack closure and crack tip plasticity

In this work, fatigue crack growth in a single crystal of a nickel based superalloy, Haynes 230, is investigated at room temperature to provide an accurate analysis of the crack growth mechanisms acting at the tip of a flaw both with an experimental approach (DIC) and numerical simulations (crystal plasticity).

In his analytical work, Williams [14] described the stress field around a crack tip, in an elastic and isotropic body, with a power law series, discovering that the singularity is of the order

---

* Corresponding author.
  E-mail address: silvio.rabbolini@polimi.it (S. Rabbolini).

Nomenclature

A	rigid body rotation
B	rigid body translation
C, m	paris law coefficients
D_0, T_0, μ_0	empirical parameters for temperature dependent shear modulus
E	Young's modulus
F, F^e, F^p	deformation gradient and its elastic and plastic components
L, L_p	velocity gradient and its plastic component
N_s	number of slip systems
R	load ratio
$R_{p,0.2\%}$	yield stress
S	yield stress in the shear direction (Hill's criterion)
T	T-stress
$\bar{T}$	temperature
U	stress range reduction factor
Y	geometric factor
X, W, Z	yield stress in the principal direction (Hill's criterion)
a	crack length
a_{ij}	elastic constants
b^s	direction of the s-th slip system
n	exponent of the slip rate
n^s	normal of the s-th slip system
r	radial distance from the tip
r_p	plastic zone radius
s	s-th slip system

x, y	horizontal and vertical coordinate
w	specimen width
$\Delta\sigma$	stress range
$\Delta\epsilon_{yy}$	axial strain difference
ΔK_{eff}	effective stress intensity factor range
$\Delta K_{I,eff}$	mode I effective stress intensity factor range
Δr_p	cyclic plastic zone radius for a linear elastic material
$\Delta r_{p,EP}$	cyclic plastic zone radius for an elastic–plastic material
$\dot{\gamma}_0$	reference slip rate
$\dot{\gamma}^s$	slip rate along the s-th slip system
$\dot{\epsilon}$	strain rate
ϵ_p	accumulated plastic strain
ϵ_{yy}	vertical strain
μ	shear modulus
σ_{open}	stress corresponding to the opening value
σ_x, σ_y	stress in the x and y direction
$\bar{\tau}$	accumulated plastic strain dependent component of $\tilde{\tau}$
$\tilde{\tau}$	slip system strength
τ_a	temperature and rate invariant component of the yield stress
τ^s	resolved shear stress
$\tau_{xy}, \tau_{yz}, \tau_{xz}$	shear stresses
τ_y	temperature and rate dependent component of the yield stress
θ	angular coordinate from the tip

$\sigma_{i,j} \propto K/r^{-1/2}$, where r is the radial distance from the tip, and that the stress intensity factor, K, is a measure of the singularity itself. Studying the singularity field for a crack in an anisotropic body, Sih et al. [15] found the singularity to be of the same order.

Initial works [16,17] employed DIC to study the effects of crack closure, by measuring the relative displacements of crack flanks during a load cycle, following Elber proposal [18]. Full field displacements were employed by McNeill et al. [19] to extract stress intensity factors with a regression technique based on the analytical singular field. Carroll et al. [20] modified the regression algorithm, including the effects of the T-stress, the second term of the power series proposed by Williams. Recently, DIC was applied to study fatigue crack growth of Haynes 230 at high temperature [21] and to study fatigue crack growth in 316L steel and Haynes 230 single crystals [22,23].

Starting from DIC-extracted stress intensity factor ranges, it is possible to evaluate the stress field acting at the tip. The stress distribution, together with an adequate yield criterion, can be used to evaluate the plastic zone, the region around the tip in which material locally yields. An initial estimation of the extent of the plastic zone in an isotropic elastic/perfectly plastic material was given by Irwin [24], who calculated the plastic zone radius, r_p, as a function of the applied stress intensity factor and of the yield stress, $R_{p,0.2\%}$. The influence of T-stress on plastic zone size was initially studied by Gao et al. [25], who observed that the influence of this term becomes significant only at moderate stress levels. Inside the plastic zone, a limited area experiences reversed plastic flow during each load cycle. Rice estimated that the radius of this region, also referred as cyclic plastic zone, is a quarter of the monotonic plastic zone [26]. McClung and Sehitoglu [27,28] discovered that the size of the cyclic plastic zone depends on crack closure.

As for numerical approaches, the plastic wake generation and crack closure (as a result of the irreversible plastic deformations at the tip of a growing crack) have been largely studied with numerical models based on a node release technique. Newman [29] simulated crack propagation in a center-crack panel by chang-

ing the stiffness of spring elements placed along the crack flanks, considering an elastic/perfectly plastic material. Following this approach, McClung and Sehitoglu [27,28] were able to study crack closure changes during crack propagation from a notch for different steels and to check the dependency of the opening stresses on the model mesh. The same approach was applied by Pommier et al. [30,31] to study the effects of material hardening on crack tip plastic zone. All these approaches were developed on 2D-models, imposing a node release at the peak stress of every load cycle. In [32], a numerical investigation of crack closure performed on a 3D model is discussed, in order to highlight the differences in crack opening levels along the front of a Mode I loaded crack. Simulations were performed on an innovative software, Warp3D [33], which allows the development of cracked models taking into account large displacement theory. In this work, crack closure is investigated with Warp3D, since the software allows the development of models that consider single crystal behavior.

1.2. Overview

This study deals with the analysis of crack propagation in a single crystal, with the aim to provide a more accurate understanding of crack growth mechanisms in individual grains. In the first part of the paper, a discussion of material properties and experimental procedures are reported together with crack growth measurements. At first, DIC measurements were used for determining closure levels and the cyclic plastic region at the crack tip.

In the following sections, experimental results, obtained with DIC, are compared to the numerical ones, obtained considering crystal plasticity. The results of the simulation performed on a quasi-static model are initially presented, with the aim to provide an initial assessment of the plastic zone. In the final part of the paper, crack closure in single crystals is studied with a model which considers crack advancement with a node release technique. Finally, numerical opening levels are implemented in a crack prop-

agation model and are compared to experimental results in terms of crack length vs cycles.

2. Experiments

2.1. Material properties

Haynes 230, a commercial Ni-based superalloy, was used during the experiments presented in this work. Haynes 230 is a solution strengthened alloy, which exhibits high resistance to corrosion, oxidation and creep, properties that makes it the preferable choice for applications in the energy and aerospace industries, such as gas turbines and combustors. High temperature properties of this superalloy are due to the addition of chromium, tungsten and molybdenum. Haynes 230 chemical composition is reported in Table 1.

Single crystals were obtained from a seed: Bridgman technique in vacuum was adopted in this phase. Crystal initial orientation was determined with electron backscatter diffraction (EBSD). Specimens were extracted from slices cut parallel to the $\{1\bar{1}0\}$ plane: this plane was chosen because it included the crystallographic orientation of interest, i.e. $[001]$, and the $[111]$ orientation. Single edge notch specimens were electrical discharge machined (EDM) from these slices: 'dog-bone' specimen geometry was adopted in this work. A schematic of the specimen is reported in Fig. 1, whereas mechanical properties of the single crystals, evaluated testing unnotched specimens, are reported in Table 2.

Before testing, EBSD was performed on the specimen to check its orientation. The loading direction was confirmed, whereas it was determined that the notch and the thickness directions were, respectively, $[3\,4\,0]$ and $[4\,\bar{3}\,0]$.

2.2. Fatigue testing and DIC procedure

Before testing, the $[001]$-oriented single crystal specimen was accurately prepared: the first step consisted in polishing the measurement surface to a mirror finish with abrasive paper. The specimen was then airbrushed with black paint: this procedure was performed to generate a speckle pattern, necessary for digital image correlation measurements. The sample was cyclically loaded in a servo-hydraulic testing machine at a frequency of 5 Hz, with a load ratio R equal to 0.05. The applied stress ratio, $\Delta\sigma$, was set to 133 MPa.

During the experiment, an high definition digital camera, whose resolution was 1600 by 1200 pixel at a rate of 15 fps, monitored the notch region. A 12X adjustable lens and a 2X adapter were employed to achieve a resolution of 0.63 μm/pix, necessary to obtain accurate measurements.

Once a crack was observed, a measurement cycle at a frequency of 0.25 Hz was performed, to get more pictures, necessary to characterize the fatigue load cycle. A computer controlled both the load frame and image acquisition, allowing the identification of the applied load, measured by a 7.5 kN load cell, for each picture.

The displacement field around the tip was characterized with Digital Image Correlation. Pictures were correlated with a commercially available software, VIC 2D by Correlated solutions. The reference image, the picture respect to all the displacements were

calculated, was taken at the minimum applied load, meaning that the displacement field was calculated with respect to the fully closed crack configuration. Further details on the experiments can be found in [23].

The strain field was computed from DIC measured displacements. Lagrange strain tensor equations were employed to calculate strains: in order to obtain a smooth field, the displacements were locally approximated with a first order polynomial. In Fig. 1, the vertical strain field measured around a 0.955 mm long crack at the maximum applied load is reported: the crack propagated in the $[001]$ plane and presented a symmetric plastic zone. This is due to the fact that, during propagation, two different slip systems were simultaneously activated. Strains are concentrated along two bands, corresponding to the directions of the traces of the slip planes activated during propagation. The highest value of the vertical strain, registered at the tip, is higher than 1%.

2.3. Crack closure measurements with DIC

In order to measure crack opening loads, a series of two points digital extensometers was placed along crack flanks. This feature tracks the relative displacements of two groups of points, also called subsets, belonging to the opposite faces of the crack: opening was evaluated by placing digital extensometers perpendicular to the crack plane and by considering the difference in the vertical crack tip displacements, as proposed in Fig. 2a. An example of the evolution of the crack profile during a single load cycle is reported in Fig. 2b, whereas the evolution of crack opening levels during the test is reported in Fig. 2c [23], in which it can be noted that, at $R = 0.05$, the ratio between the opening and the maximum stress kept constant and equal to 20%. A more accurate description of crack closure measurements is reported in [23].

3. Cyclic plastic zone from the displacement field

DIC provides the displacement field in the tip region, which can be used to evaluate crack driving forces without geometric considerations. In [22,23], a non-linear least squares algorithm was implemented and successfully employed to extract crack propagation driving forces, in terms of the effective stress intensity factors, ΔK_{eff}, and to observe how these values progress during a single load cycle. The algorithm extracted ΔK_{eff} by fitting DIC displacements with the analytical singular field, which considered material anisotropic behavior.

The analytical singular field for a crack in an anisotropic body, adopted in the regression algorithm, is reported in Eq. (1) [15,34], in which v are the displacements in the direction normal to crack plane, Re denotes the real part of a complex number, r and θ are the coordinates of a point expressed in a polar system centered at the tip, a_{ij} are the elastic constants of nickel, as proposed by Hertzberg in [35], T is the T-stress, A and B are terms that accounts for rigid body rotation and translation, μ_1 and μ_2 are the two complex conjugate roots of Eq. (2), for which the imaginary parts are positive, and q_i are complex numbers computed as proposed in Eq. (3).

$$v = \Delta K_{I,eff}\sqrt{\frac{2r}{\pi}}Re\left[\frac{1}{\mu_1 - \mu_2}\left\{\mu_1 q_2\sqrt{cos\theta + \mu_2 sin\theta}\right.\right.$$
$$\left.\left. - \mu_2 q_1\sqrt{cos\theta + \mu_1 sin\theta}\right\}\right] + a_{12}Trsin\theta + Arcos\theta + B \tag{1}$$

$$a_{11}\mu^4 - 2a_{16}\mu^3 + (2a_{12} + a_{66})\mu^2 - 2a_{26}\mu + a_{22} = 0 \tag{2}$$

$$q_i = a_{12}\mu_i + \frac{a_{22}}{\mu_i} - a_{26} \tag{3}$$

Table 1
Chemical composition (%wt) of Haynes 230.

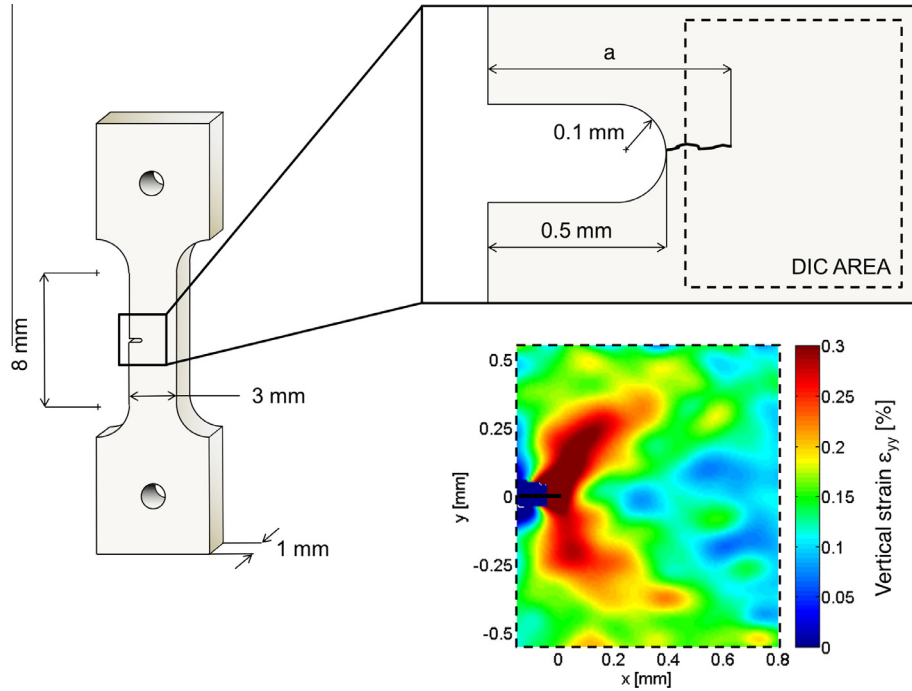| Al	B	C	Co	Cr	Cu	Fe	La	Mn
0.35	0.005	0.1	0.16	22.14	0.04	1.14	0.015	0.5
Mo	Ni	P	S	Si	Ti	W	Zr	
1.25	Bal.	0.005	0.002	0.49	0.01	14.25	0.01	

Fig. 1. Fatigue crack growth analysis with DIC. Geometry of the 'dog-bone' specimen and definition of the region of interest, together with the vertical strain field registered at the maximum applied load around the tip of a 0.955 mm long crack.

Table 2
Tensile properties of Haynes 230 single crystals loaded along different directions.

Loading direction	$R_{p,0.2\%}$ (MPa)	E (MPa)
[0 0 1]	274	137
[1 1 1]	428	330

The regression algorithm calculated the set of variables necessary to fit the experimental field, using Eq. (1). In Fig. 3a, experimental displacements registered at the tip of a 0.955 mm long crack at the maximum applied load are compared to those obtained from regression, represented in blue. Crack profile and crack tip are represented by a black line and a black dot. The regression algorithm is capable of describing the singularity in the crack tip region, showing a good agreement between theory and experiments. Further details on the regression algorithm and on ΔK_{eff} extraction can be found in [22,23].

The evaluation of the crack propagation driving forces allowed the definition of the stress field around the tip: in this work, the stress distribution around the tip was computed considering material anisotropic behavior and plane stress conditions, since the specimen is thin [15]:

$$
\begin{cases}
\sigma_x = \frac{\Delta K_I}{\sqrt{2\pi r}} F_{Ix} = \frac{\Delta K_I}{\sqrt{2\pi r}} Re\left[\frac{\mu_1 \mu_2}{\mu_1 - \mu_2}\left(\frac{\mu_2}{\sqrt{\cos\theta + \mu_2 \sin\theta}} - \frac{\mu_1}{\sqrt{\cos\theta + \mu_1 \sin\theta}}\right)\right] \\
\sigma_y = \frac{\Delta K_I}{\sqrt{2\pi r}} F_{Iy} = \frac{\Delta K_I}{\sqrt{2\pi r}} Re\left[\frac{1}{\mu_1 - \mu_2}\left(\frac{\mu_1}{\sqrt{\cos\theta + \mu_2 \sin\theta}} - \frac{\mu_2}{\sqrt{\cos\theta + \mu_1 \sin\theta}}\right)\right] \\
\tau_{xy} = \frac{\Delta K_I}{\sqrt{2\pi r}} F_{Ixy} = \frac{\Delta K_I}{\sqrt{2\pi r}} Re\left[\frac{\mu_1 \mu_2}{\mu_1 - \mu_2}\left(\frac{1}{\sqrt{\cos\theta + \mu_1 \sin\theta}} - \frac{1}{\sqrt{\cos\theta + \mu_2 \sin\theta}}\right)\right]
\end{cases}
\tag{4}
$$

The plastic zone around the tip was calculated combining the analytical singular stress field (Eq. (4)) with a yield criterion that accounted for single crystal anisotropic behavior. In this work, the extension proposed by Hill of Von Mises' yield criterion was used [36]. The yield criterion in quadratic form can be expressed as:

$$
D(\sigma_y - \sigma_z)^2 + G(\sigma_z - \sigma_x)^2 + H(\sigma_x - \sigma_y)^2 + 2M\tau_{xy}^2 + 2N\tau_{xz}^2 + 2O\tau_{yz}^2 = 1
\tag{5}
$$

where D, G and H are coefficients that characterize material anisotropy in the normal directions and M, N and O are the coefficients that define shear anisotropy. These constants can be calculated as reported in Eq. (6), in which X, Y and Z are the yield stresses in principal directions and S is the shear yield stress.

$$
\begin{cases}
2D = -\frac{1}{X^2} + \frac{1}{W^2} + \frac{1}{Z^2} \\
2G = \frac{1}{X^2} - \frac{1}{W^2} + \frac{1}{Z^2} \\
2H = \frac{1}{X^2} + \frac{1}{W^2} - \frac{1}{Z^2} \\
2M = \frac{1}{S^2}
\end{cases}
\tag{6}
$$

Assuming plane stress, $\sigma_z = \tau_{xz} = \tau_{yz} = 0$, Eq. (5) can be rewritten as:

$$
(G+H)\sigma_x^2 - 2H\sigma_x\sigma_y + (D+H)\sigma_y^2 + 2M\tau_{xy}^2 = 1
\tag{7}
$$

The extension of the plastic zone is obtained by substituting Eq. (4) into Eq. (7) and solving for the plastic zone radius, r_p. In this work, the attention is focused on the cyclic plastic zone, the process zone in which reverse yielding occurs. As suggested by Rice [26], the extension of the cyclic plastic zone can be approximately evaluated by considering one quarter of r_p, as reported in Eq. (8).

$$
\begin{aligned}
\Delta r_p &= \frac{1}{4}r_p \\
&= \frac{\Delta K_{I,eff}^2}{8\pi}\left[(G+H)F_{Ix}^2 - 2HF_{Ix}F_{Iy} + (D+H)F_{Iy}^2 + 2MF_{Ixy}^2\right]
\end{aligned}
\tag{8}
$$

In Fig. 3b, the cyclic plastic zone, computed according to Eq. (8) is represented by a dashed black line and is compared to the experimental strain field. Differently from the round shape observed in polycrystals, the anisotropic cyclic plastic zone of a crack loaded under pure Mode I showed two marked lobes extending from the
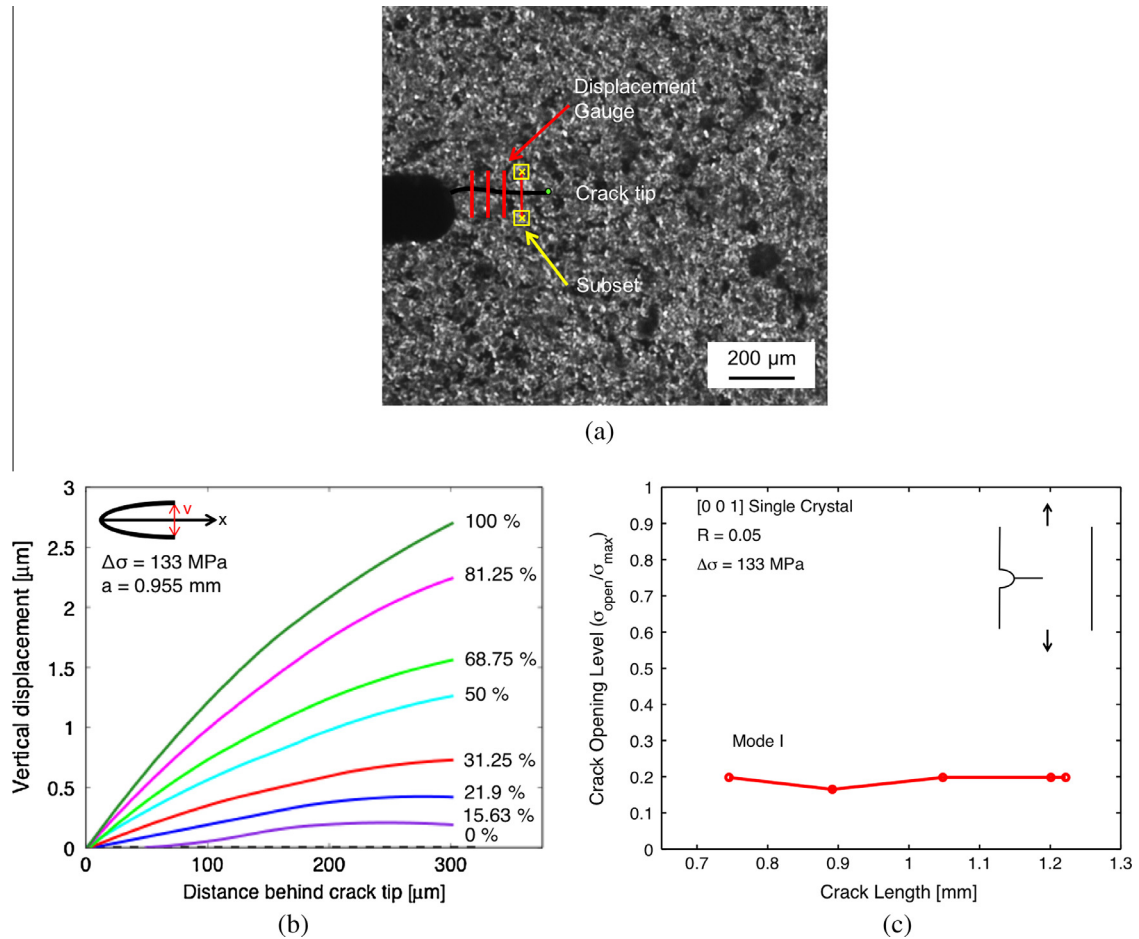
Fig. 2. Crack closure measurements with DIC. (a) disposition of the digital extensometer along the crack; (b) vertical crack opening displacement profiles of the [0 0 1] single crystal at R = 0.05 and $\Delta\sigma = 133$ MPa with a measured crack length of 0.955 mm. (c) Crack opening levels measured during the crack propagation test [23].
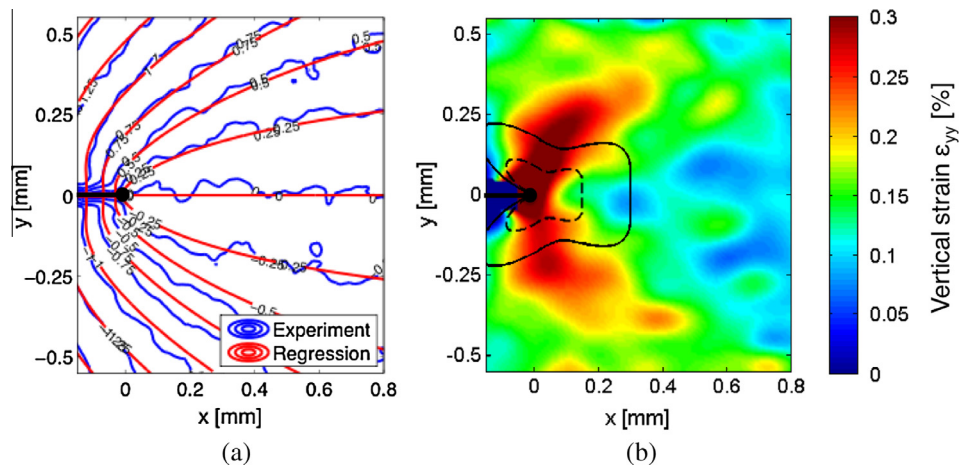

Fig. 3. Cyclic plastic zone analysis with DIC for a 0.955 mm long crack in the [0 0 1] oriented single crystal. (a) Comparison of experimental and regressed vertical displacement contours in micrometers. $\Delta K_{I,eff}$ from regression is equal to 13.49 MPa$\sqrt{m}$; (b) comparison between experimental strains and the cyclic plastic zone calculated according to Hill. The dashed line represents the cyclic plastic zone calculated from Eq. (8), whereas the continuous line represents the cyclic plastic zone calculated according to Eq. (9).

tip towards crack flanks. This is in contrast with experimental observations, since the strains were accumulated along the direction of the activated slip systems. The extension of the cyclic plastic zone, calculated according to Eq. (8), is equal to 0.0345 mm^2.

The difference in extension of the cyclic plastic zone is due to the fact that, in these calculations, only material elastic behavior was taken into account. The presence of plastic strains can be implemented following Irwin's suggestions [24]: material elastic/

perfectly plastic behavior involves a stress redistribution at the tip, with an increase of the plastic zone radius, which can be roughly estimated as the double of the value calculated from linear elastic fracture mechanics. Therefore the cyclic plastic zone radius in case of a elastic/perfectly plastic material can be calculated as:

$$\Delta r_{p,EP} = 2\Delta r_p$$
$$= \frac{\Delta K_{I,eff}^2}{4\pi} \left[(G+H)F_{Ix}^2 - 2HF_{Ix}F_{Iy} + (D+H)F_{Iy}^2 + 2MF_{Ixy}^2 \right] \quad (9)$$

In Fig. 3b, the cyclic plastic zone, computed according to Eq. (9) is represented by a black continuous line. The adoption of Irwin equation implies a change in the cyclic plastic zone extension, which, in this case, is equal to 0.1461 mm^2.

4. Cyclic plastic zone from crystal plasticity simulations

In this work, numerical simulations based on crystal plasticity were performed in Warp3D [33]. In this section, a brief description of the crystal plasticity model implemented in Warp3D is presented, together with the discussion of the results obtained from two numerical models of the cracked specimen: the effects of single crystal behavior are initially investigated in a quasi-static model, whereas the effects of crack closure and strain accumulation are analyzed with a model which simulated crack propagation with a node release technique.

4.1. Overview of the crystal plasticity code employed in Warp3D

Constitutive models with CP concepts have the objective to describe inelastic deformation in terms of the amount of slip occurring in each crystallographic slip system. The CP implementation in Warp3D consists of the description of crystal kinematics [4–7] together with the definition of a constitutive relation for slip system hardening. The kinematics problem can be defined considering three different configurations of the continuum body: reference, intermediate/unrotated, current (see Fig. 4a). The changes from one configuration to the following one is related to the deformation gradients: F^e describes the part associated to the elastic deformation of the lattice, whereas F^p is the term that accounts for plastic deformation. In this scheme, the total deformation gradient, F, is not given by the sum of F^e and F^p, but by their product, following the multiplicative decomposition concept originally proposed by Lee [37]:

$$F = F^e F^p \quad (10)$$

From Eq. (10) it is possible to determine the velocity gradient as $L = \dot{F}F^{-1}$; its decomposition is symmetric and skew components allow to define the stress rate that has to be integrated in Warp3D [33].

The velocity gradient formulation for a single crystal assumes that plastic straining is only related to slip occurring in slip systems. Accordingly, the plastic component of L can be expressed through the scalar product:

$$L_p = \sum_{s=1}^{N_s} \dot{\gamma}^s b^s \otimes n^s \quad (11)$$

where b^s and n^s denote direction and normals of the s-th slip plane in the lattice frame and $\dot{\gamma}^s$ is the slip rate along each system.

The slip rate depends on the reference strain rate ($\dot{\gamma}^0$), the resolved shear stress ($\tau^{(s)}$) and the slip system strength ($\tilde{\tau}$). In Warp3D, it is assumed that slip system hardening is isotropic and that all slip systems have the same strength. Hence, the definition of the slip rate for each slip system is defined as:

$$\dot{\gamma}^s = \frac{\dot{\gamma}_0}{\tilde{\tau}} \left| \frac{\tau^s}{\tilde{\tau}} \right|^{n-1} \tau^s \quad (12)$$

In Warp3D, hardening is modeled with a Mechanical Threshold Stress model (MTS) [38,39]. The slip system strength ($\tilde{\tau}$) follows the formulation of the MTS model in its form:

$$\tilde{\tau} = \tau_a + \tau_y(\overline{T}, \dot{\epsilon}) \frac{\mu(\overline{T})}{\mu_0} + \bar{\tau}(\epsilon_p, \overline{T}, \dot{\epsilon}) \frac{\mu(\overline{T})}{\mu_0} \quad (13)$$

with $\mu(\overline{T}) = \mu_0 - \frac{D_0}{exp(\overline{T}/T_0) - 1}$. τ_a and τ_y are yield stress components, the first one is a constant while the second is temperature and rate dependent, whereas $\bar{\tau}$ depends on the accumulated plastic strain, other than temperature and rate (see Fig. 4b). Elastic properties dependency is defined through the $\frac{\mu(\overline{T})}{\mu_0}$ ratio.

4.2. Quasi-static model

An initial assessment of crack tip plastic zone was obtained by considering the crack as stationary, neglecting the effects of plastic wake during propagation. The model, depicted in Fig. 5, reproduced the dog-bone specimen geometry of Fig. 1 with a 0.955 mm long crack and was constrained to fully reproduce
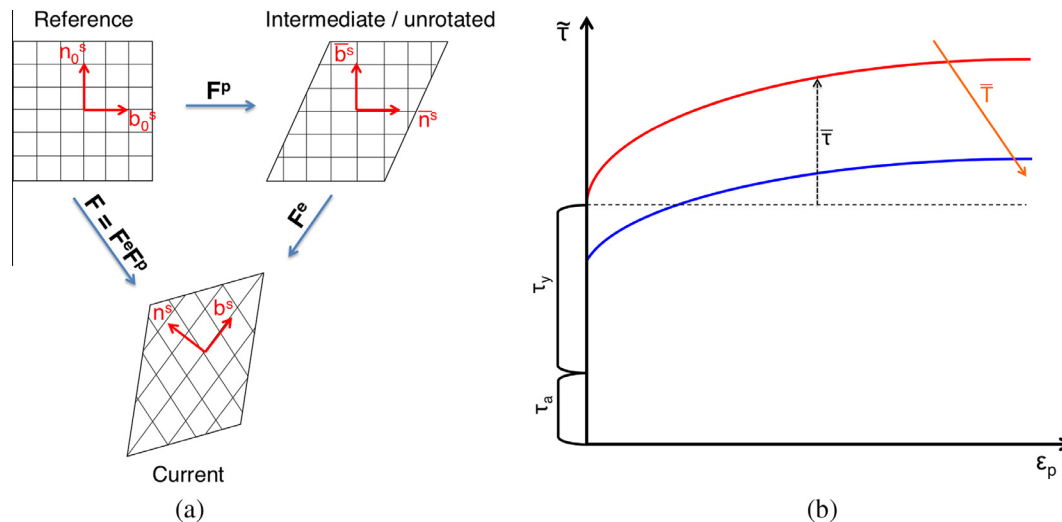

Fig. 4. Crystal Plasticity model: (a) schematic of crystal's Kinematic with multiplicative decomposition of $F = F^e F^p$; (b) Behavior of the slip system hardening model Eq. (13).
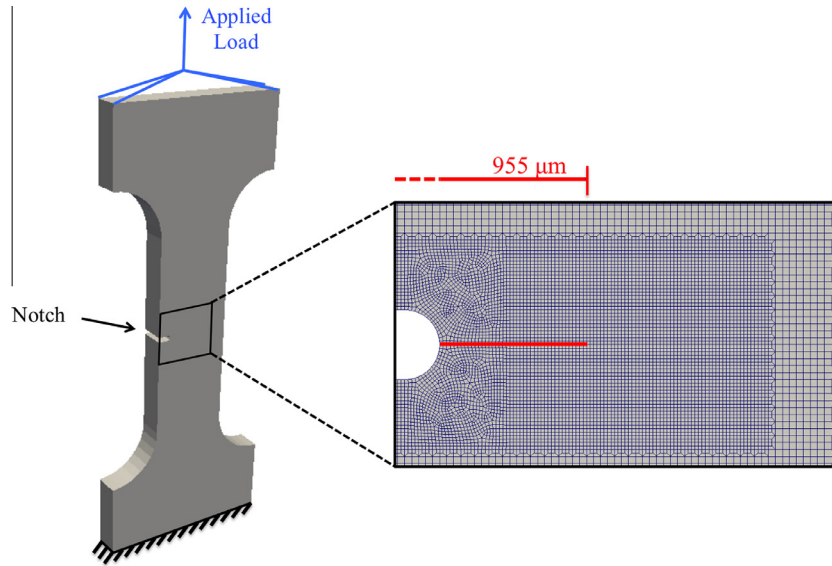
Fig. 5. Quasi-static crack finite element model for the [0 0 1] oriented specimen, with a close-up view of the mesh around the crack.

experimental conditions: an encastre neglected all the displacements of the bottom face, whereas the force was applied, through a coupling constraint, on the upper surface of the model. In order to accurately describe the strain field ahead of the tip, 8-node 3D isoparametric elements with a dimension of 1% of model thickness were employed during the analysis.

The quasi-static model was developed neglecting the effects of crack growth and closure. Accordingly, the applied load was modified respect to the experimental one, in order to keep the crack always open and to apply the experimentally measured effective stress intensity factor range. In order to consider both these conditions, the model was cyclically loaded between the maximum and the opening load, as reported in Fig. 6a.

DIC does not provide an absolute measurement of strains. All the strains are calculated respect to the reference image, which is the image taken at the minimum applied load. Therefore, the strain field reported in Fig. 1 is the difference between the strain field at the peak and at the minimum load. Thus, a comparison between FEM and DIC results is possible only if the difference between the strains computed at the peak and at the opening stress are taken into account. In Fig. 6b, the evolution of axial strains difference, $\Delta\epsilon_{yy}$, during six consecutive cycles is reported (this six cycles are those from Fig. 6a, the strain differences are between point 4 and 3 for the first cycle, 6 and 5 for the second and so on for the others): a major difference between the first cycle and the following ones is highlighted, whereas convergence is achieved only after the fifth cycle.

Finally, a comparison between experimental and numerical results is reported in Fig. 7, in which it can be noted that the extension of the plastic zone is quite different, whereas a good agreement in terms of bands orientation is obtained. These observations leads to the conclusion that a quasi-Static model cannot completely represent a fatigue crack: the assumption of neglecting the plastic wake, and the subsequent crack closure
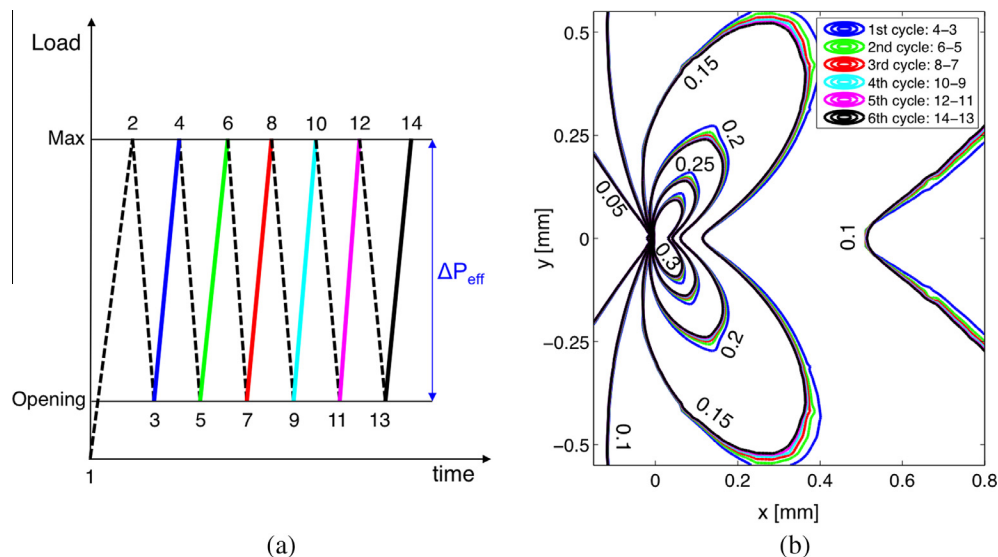

Fig. 6. Strain field convergence in quasi-static crack analysis for a crack of 0.955 mm. (a) loading history of the QS model considering 6 cycles: the load is kept, after the first ramp, between the maximum and the opening level. (b) Strain field contours (strains are in percentage) for each cycle to analyze results convergence.
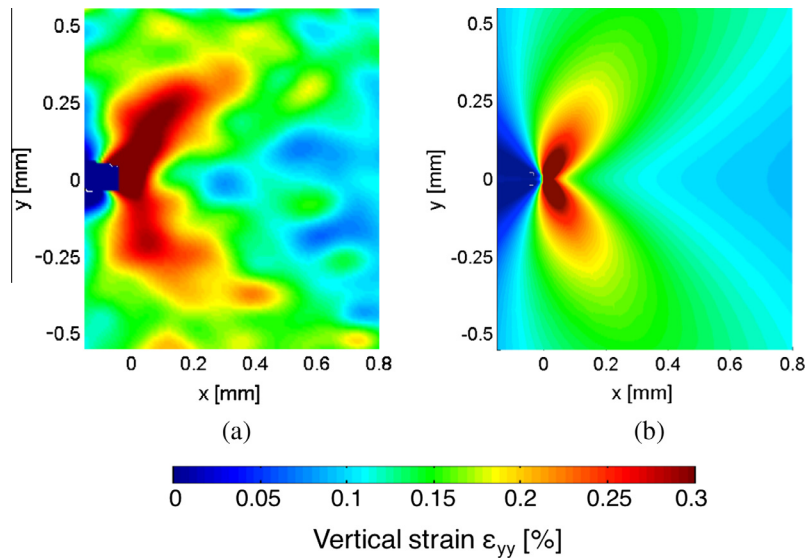
Fig. 7. Comparison between experimental strain field measurements and the quasi-static simulation at the 6th cycle for a crack length of 0.955 mm.

effect, is the main limit of this model, since it removes from the simulation the irreversibility and the strain accumulation present ahead of the tip, in the plastic wake, during fatigue crack growth.

4.3. Propagating crack model

The analysis performed on the quasi-static model gave an idea of CP model capabilities in terms of slip angles identification and numbers of cycles necessary to reach strain field convergence. This information was employed to develop an enhanced model, in which the effects due to crack growth were taken into account. In order to numerically reproduce the plastic wake, a node release technique was implemented. This technique consists in simulating crack propagation, by releasing, during each load cycle, all the nodes belonging to the current crack front, in the first unloading step after the maximum load. Accordingly, the crack advances uniformly over the thickness during the simulation, by an amount equal to the element size.

To analyze crack opening during the propagation, a model with a small precrack has been implemented. Transition crack length after wich the notch the SIF is not influenced by the notch effect can be estimated as $0.13\sqrt{L_{notch}R_{notch}}$ (where L_{notch} and R_{notch} are notch length and its radius) [40]. Accordingly, a precrack of 30 μm has been modeled at the notch root for nodal release simulations.

The element size in the crack region, corresponding to the discrete crack advancement considered during the simulation, was set equal to 0.01 mm considering the relationship between element size (Δa) and the plastic radius (r_p) [27], that states $\Delta a/r_p \leqslant 0.05$. a close up of the mesh in the crack region is reported in Fig. 8, in which the geometry used in the simulation is also reported. In order to reduce computational times, all the present symmetries were taken into account. Two symmetry planes were considered, meaning that only one quarter of the specimen was modeled. Accordingly, boundary conditions were modified respect to the quasi-static model: symmetries were modeled by neglecting displacements along the direction normal to the symmetry plane, whereas a coupling constraint in the upper surface was employed to apply the remote load.

In this simulation, the specimen was cyclically loaded between the maximum and minimum applied stress. The load cycle was divided in variably sized increments, as reported in Fig. 8: the small increments defined at the start of the cycle were necessary to provide better resolution and to detect the opening load. Another step refinement was considered after the peak load, the point in which node release occurred: this feature was necessary to insure full redistribution of the reaction forces acting on the released nodes. Finally, another step refinement was placed in the final part of the cycle, to avoid numerical errors occurring during crack flanks contact.

Considering the results of the convergence analysis presented in Section 4.2, three different strategies were taken into account: a release every cycle, every two cycles and every five cycles. With these three load histories it was possible to analyze strain field convergence even for this case. To reproduce the experimental observation reported in Section 3, in this case it is necessary to compute the difference between the strains registered at the peak and the valley load, since the effects of crack closure were included even in the numerical model. In Fig. 9, the vertical strain registered at the end of the simulation for all the three different node release histories is reported: from this comparison it is evident that the strain field variation is not as much highlighted as in the stationary crack case. Accordingly, it is possible to assume that the differences between the results with a node release every cycle and every 5 cycles are negligible in terms of strain field.

Crack opening levels were calculated following the procedure described in [30,31] and depicted in Fig. 10a: the ratio between the variation of the displacement of the second node behind the tip and the maximum displacement of that node was plotted against the applied stress. The crack was assumed to be open when this ratio was equal to 1.5%. It was found that crack opening levels for the 0.955 mm long crack depend on the number of cycles between each node release: when crack advancement occurred every cycle, the opening level registered was equal to 19.4% of the peak stress. Opening was observed at a lower stress level when the model with a release every 2 cycles was considered: in this case the percentage was equal to 18.3%. A less marked drop was measured when the model with a crack advancement every 5 cycles was taken into account: the ratio between the opening stress and the maximum one was equal to 17.8%. The difference between the model with an advancement every cycle and the one that considered crack propagation every 5 cycles was lower than 10%, meaning that a good estimate of crack opening levels
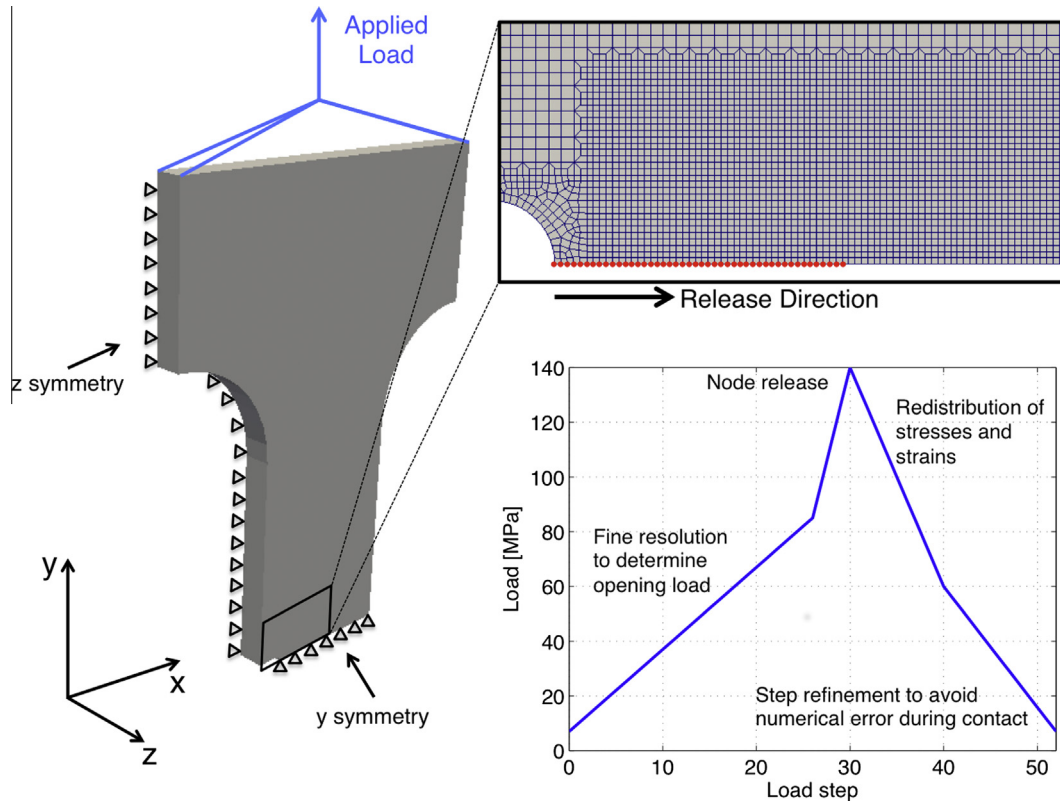
Fig. 8. Propagating crack FE model for [0 0 1] specimen: model loading conditions and symmetry constraints; highlight of the crack and the nodes that are released during the simulation; details of a load cycle, variable load steps are adopted to accommodate node release, redistribution of stresses and strains and contact.
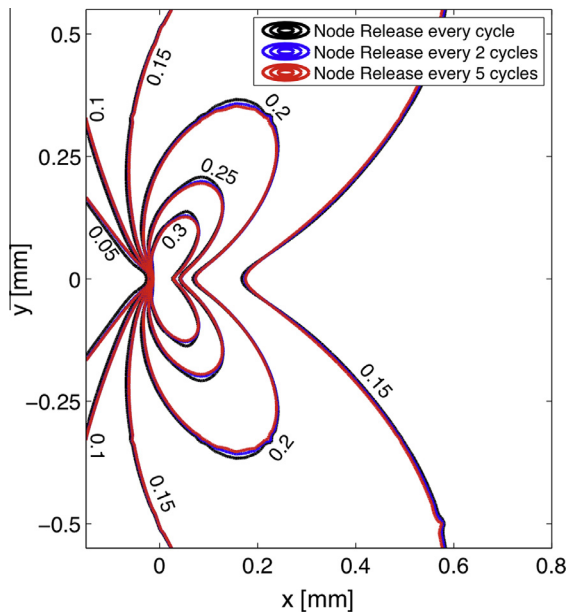

Fig. 9. Node release model, plastic zone analysis of the 0.955 mm long crack: comparison between the strain field contours for each node release strategy. Strains are expressed in %.

can be obtained even with a model which considers a limited number of load cycles, as reported in Fig. 10b, in which a good agreement between experimental and FEM opening levels can be observed; in the same figure, for the release every 5 cycles, the history of the opening level is registered at discrete crack length (0.55, 0.6, 0.7, 0.8, 0.9, 0.955 mm).

The attention was then shifted on the study of the capabilities of the model to describe the plastic wake region and its effect on σ_{open}, as reported in Fig. 11, in which the results of the model with the precrack and a node release every 5 cycles are reported. In Figs. 11a–c, the strain field registered at the peak stress of three different crack lengths (0.7, 0.9 and 0.955 mm) is reported, in which it can be noted that the crack tip plastic zone is increasing during propagation. To have a good view of the crack opening values and the augmentation of the hysteretic behavior of the material, the remote applied stress is plotted against the displacement at a node behind crack tip (as described in Fig. 10a). in Figs. 11d–f, the entire loading cycle has been considered for the 3 different crack length. Fig. 11d shows an opening level of 23% for a crack length of 700 μm, with a cycle that shows low hysteresis. Figs. 11e–f show an higher hysteresis and a regime opening value around 18%, as shown in Fig. 10b.

Fig. 12 is a summary of the results achieved with the simulation that considered five cycles between each release. In Fig. 12a, the vertical strain field is reported: a larger strain concentration can be observed at the tip, meaning that strain accumulation is the main cause of the wrong assessments provided by the quasi-static model. The model correctly describes plastic zone shape and extension (Fig. 12a and b). A good agreement between numerical and experimental results was observed even when vertical displacements were taken into account (Fig. 12c), meaning that the model is capable of describing not only the process zone, but also those points outside the singular region.

5. Fatigue life assessment

Numerical results provided an assessment of crack opening levels. These levels, together with a closure-free crack propagation
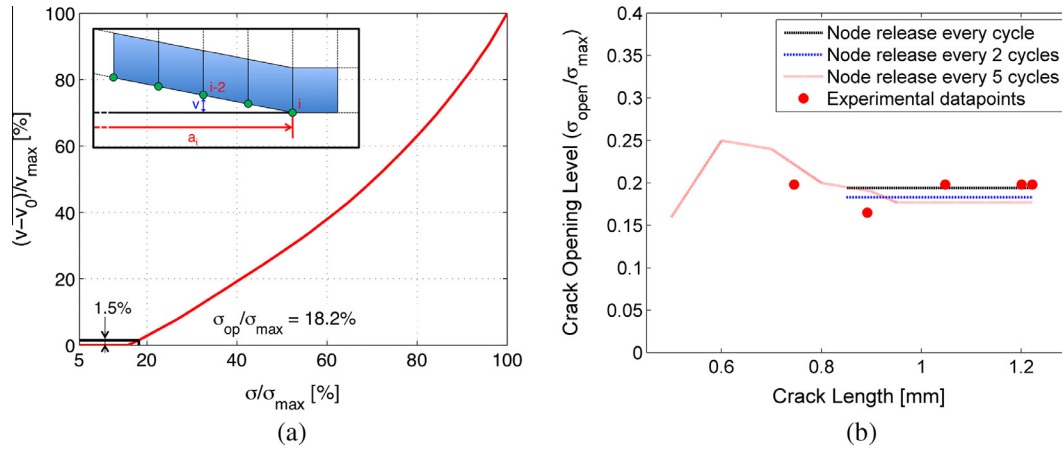
(a)   (b)

Fig. 10. Crack closure measurements on the numerical models. (a) Numerical criterion for the determination of the opening level from finite element analysis [30,31]; (b) comparison between experimental and numerical results, for 1 and 2 cycles release only the value at the maximum crack length have been recorded, for the 5 cycles various intermediate crack lengths were analyzed.
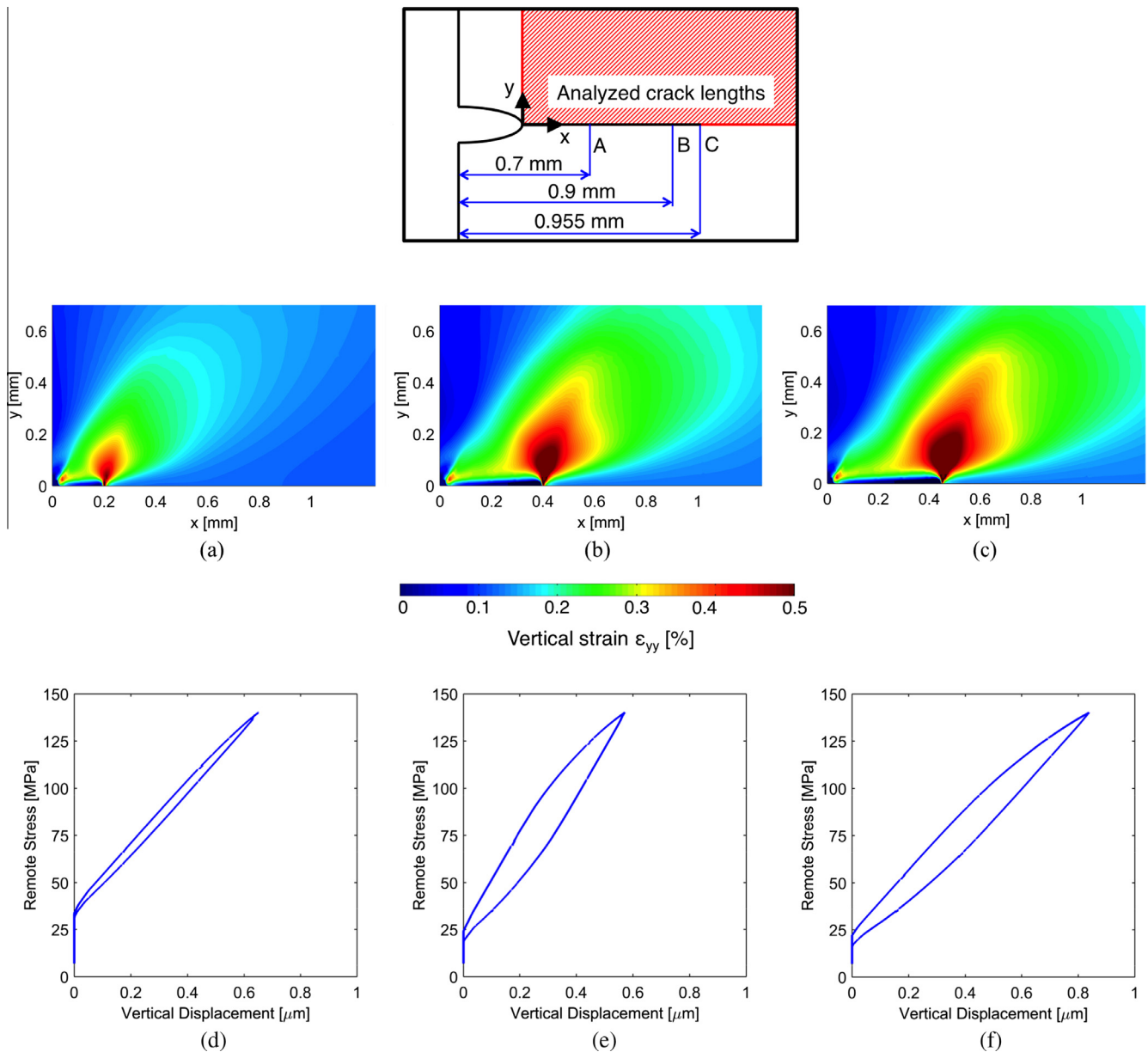

(a)   (b)   (c)

Vertical strain ε_{yy} [%]

(d)   (e)   (f)

Fig. 11. Plastic wake analysis. (a–c) Vertical strain field at the peak stress of the fatigue cycle when the crack is 0.7, 0.9 and 0.955 mm long; (d–f) remote stresses against vertical displacements measured at the second node behind crack tip for the three identified crack lengths.
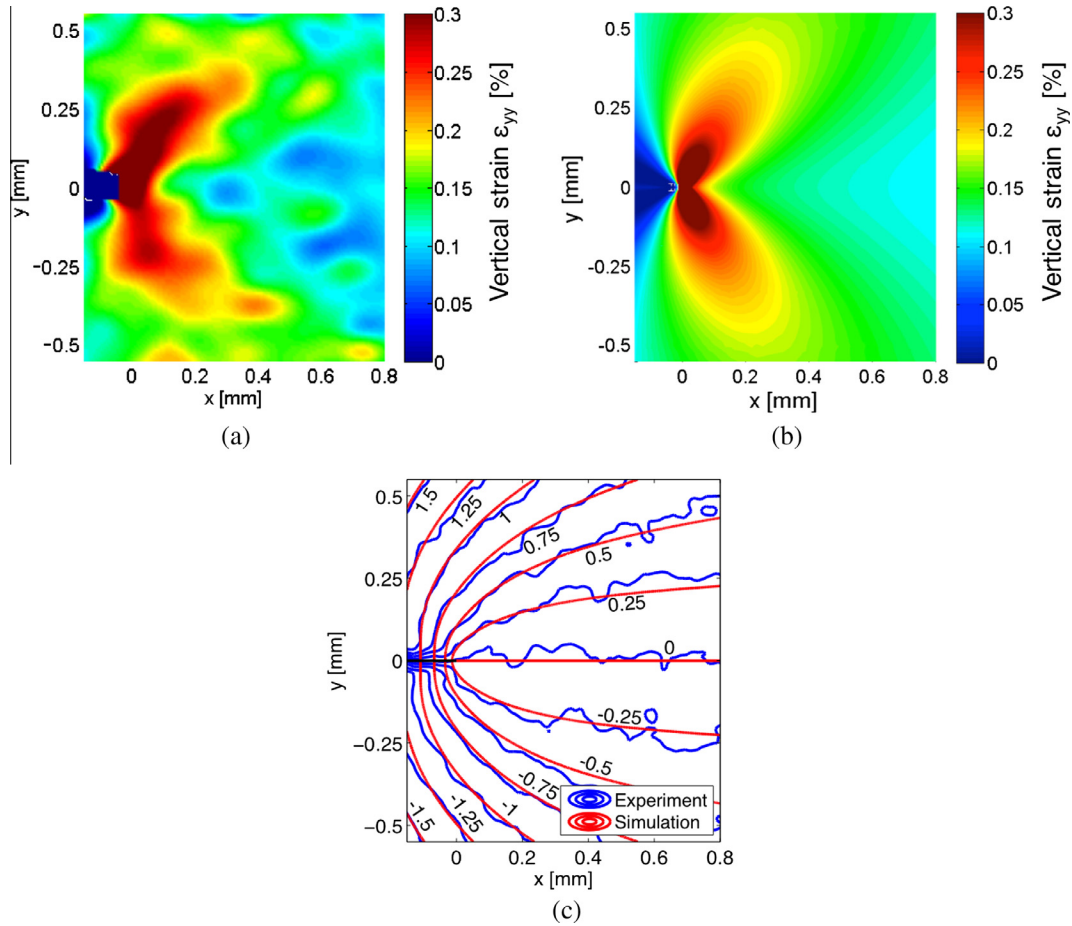
Fig. 12. Comparison between experimental and numerical results for a 0.955 mm long crack, node release model with a release every 5 cycles: (a) experimental strain field; (b) numerical strain field; (c) comparison between experimental and numerical vertical displacement fields (contours are in μm).
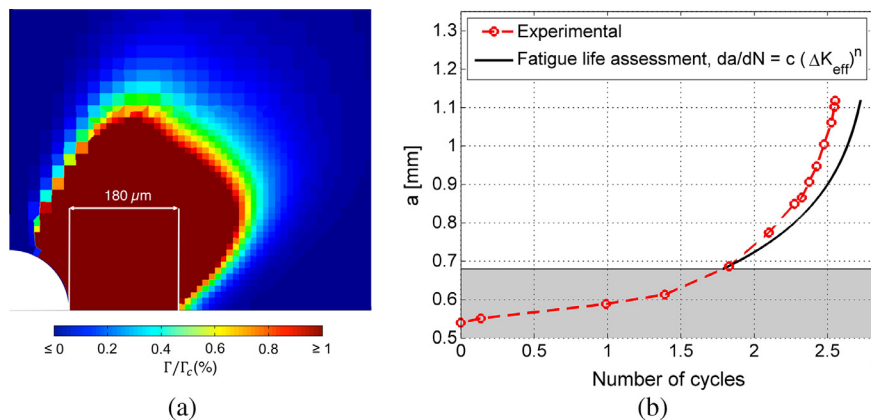

Fig. 13. Fatigue life assessment of the single crystal specimen. (a) Plastic zone around the notch at the peak stress of the first load ramp; (b) comparison between experimental results and the fatigue life assessment based on the ΔK_{eff}-propagation model.

curve can be used to develop a propagation model to simulate crack advancement in single crystal specimens. In [41], an experimental campaign on SE(B) specimens, made of Haynes 230 polycrystals, was carried out to evaluate Haynes 230 crack propagation curve in absence of closure. The effects of crack closure were removed, in those tests, by applying an high stress ratio, equal to 0.7.

In this work, the closure-free propagation curve measured in polycrystal Haynes 230 was employed to assess fatigue life of the single crystal specimen. In order to remove the effects of the notch

on propagation, a numerical simulation was performed to evaluate the size of the plastic zone generated at the notch during the first load ramp. The extension of the plastic zone was calculated following Rice's proposal [8]: a node was considered yielded when Γ, the sum of the magnitudes of the slips ($\Gamma = \sum |\gamma^s|$), was greater than 1% Γ_c, the slip at yielding, calculated as:

$$\Gamma_c = \frac{\tilde{\tau}_{(\epsilon_p=0)}}{\mu_0} \tag{14}$$

Numerical results, presented in Fig. 13a, show that the monotonic plastic zone around the notch extends for 180 μm. Accordingly, fatigue life was assessed by calculating the number of cycles necessary to the crack to propagate from an initial defect size of 0.68 mm to the final one, measured when the test was ended. An analytical procedure was implemented: the steps computed in each iteration were the following:

- calculation of the $i - th$ effective stress intensity factor range, $\Delta K_{I,eff}$ as:

$$\Delta K_{I,eff} = YU\Delta\sigma\sqrt{\pi a} \tag{15}$$

where Y is a geometric factor that accounts for specimen geometry, calculated as proposed in Eq. (16) [42], in which w is specimen width, U is the stress range reduction factor, calculated as proposed in Eq. (17), in which σ_{max} and σ_{min} are, respectively, the maximum and the minimum applied stress, and σ_{op} is the crack opening stress, calculated by FEM ($\sigma_{op} = 17.8\%\ \sigma_{max}$).

$$Y = 0.265(1 - a/w)^4 + \frac{0.857 + 0.265(a/w)}{(1 - a/w)^{3/2}} \tag{16}$$

$$U = \frac{\sigma_{max} - \sigma_{op}}{\sigma_{max} - \sigma_{min}} \tag{17}$$

- Calculation of the $i - th$ crack increment as:

$$da_i = C\big(\Delta K_{I,eff}\big)^m \cdot \widehat{dN}, \text{ with } \widehat{dN} = 1 \tag{18}$$

where C and m are the constants that describe the closure-free propagation curve presented in [41].
- Crack length update:

$$a_i = a_{i-1} + da_i \tag{19}$$

Fatigue life assessment, obtained considering $\Delta K_{I,eff}$, is represented in Fig. 13 by a black continuous line: the assessment provides good estimates. This means that fatigue crack growth, for the single crystals analyzed in this work, is driven by the effective stress intensity factor range and it can be modeled taking into account the effective crack growth curve measured in polycrystals.

6. Conclusions

In this paper, fatigue crack growth was investigated in a [0 0 1] single crystal of a Ni-based superalloy, Haynes 230. Crack propagation was characterized by digital image correlation. It was found that, in a single crystal, crack opening levels are lower than those observed in a polycrystalline aggregate. An average $\sigma_{open}/\sigma_{max}$ of 20% was observed during the experiments.

Experimental results were compared to those provided by a FEA model. Single crystal anisotropic behavior was implemented by considering an MTS model. A node release technique was employed to simulate crack propagation and to estimate crack opening levels. Numerical simulations confirmed experimental results. Experimental results were also confirmed in terms of crack tip strain fields. Excellent agreement was observed both in terms of crack tip plastic zone shape and extension.

Numerical results were employed to develop a crack propagation model based on the effective stress intensity factor range. It was found that fatigue crack growth in single crystals can be described taking into account numerical opening levels and the effective crack propagation curve measured during polycrystal testing.

References

[1] Reed RC. The superalloys: fundamentals and applications. Cambridge University Press; 2006.
[2] Duquette D, Gell M. The effects of environment on the elevated temperature fatigue behavior of nickel-base superalloy single crystals. Metall Trans 1972;3 (7):1899–905.
[3] McDowell D, Dunne F. Microstructure-sensitive computational modeling of fatigue crack formation. Int J Fatigue 2010;32(9):1521–42.
[4] Hill R. Generalized constitutive relations for incremental deformation of metal crystals by multislip. J Mech Phys Solids 1966;14(2):95–102.
[5] Hill R, Rice J. Constitutive analysis of elastic–plastic crystals at arbitrary strain. J Mech Phys Solids 1972;20(6):401–13.
[6] Needleman A, Asaro R, Lemonds J, Peirce D. Finite element analysis of crystalline solids. Comput Methods Appl Mech Eng 1985;52(1):689–708.
[7] Rice JR. Inelastic constitutive relations for solids: an internal-variable theory and its application to metal plasticity. J Mech Phys Solids 1971;19(6):433–55.
[8] Rice J, Hawk D, Asaro R. Crack tip fields in ductile crystals. In: Non-linear fracture. Springer; 1990. p. 301–21.
[9] Flouriot S, Forest S, Cailletaud G, Köster A, Rémy L, Burgardt B, Gros V, Mosset S, Delautre J. Strain localization at the crack tip in single crystal ct specimens under monotonous loading: 3d finite element analyses and application to nickel-base superalloys. Int J Fract 2003;124(1–2):43–77.
[10] Potirniche G, Daniewicz S. Analysis of crack tip plasticity for microstructurally small cracks using crystal plasticity theory. Eng Fract Mech 2003;70 (13):1623–43.
[11] Gall K, Sehitoglu H, Kadioglu Y. Plastic zones and fatigue-crack closure under plane-strain double slip. Metall Mater Trans A 1996;27(11):3491–502.
[12] Potirniche G, Daniewicz S, Newman J. Simulating small crack growth behaviour using crystal plasticity theory and finite element analysis. Fatigue Fract Eng Mater Struct 2004;27(1):59–71.
[13] Bouvard J, Chaboche J, Feyel F, Gallerneau F. A cohesive zone model for fatigue and creep-fatigue crack growth in single crystal superalloys. Int J Fatigue 2009;31(5):868–79.
[14] Williams M. On the stress distribution at the base of a stationary crack. J Appl Mech 1957;24:109–14.
[15] Sih GC, Paris P, Irwin GR. On cracks in rectilinearly anisotropic bodies. Int J Fract Mech 1965;1(3):189–203.
[16] Riddell W, Piascik R, Sutton M, Zhao W, McNeill S, Helm J. Determining fatigue crack opening loads from near-crack tip displacement measurements. ASTM Special Technical Publication 1343; 1999. p. 157–74.
[17] Sutton MA, Zhao W, McNeill SR, Helm JD, Piascik RS, Riddell WT. Local crack closure measurements: development of a measurement system using computer vision and a far-field microscope. ASTM Special Technical Publication 1343; 1999. p. 145–56.
[18] Elber W. Fatigue crack closure under cyclic tension. Eng Fract Mech 1970;2 (1):37–44.
[19] McNeill S, Peters W, Sutton M. Estimation of stress intensity factor by digital image correlation. Eng Fract Mech 1987;28(1):101–12.
[20] Carroll J, Efstathiou C, Lambros J, Sehitoglu H, Hauber B, Spottswood S, et al. Investigation of fatigue crack closure using multiscale image correlation experiments. Eng Fract Mech 2009;76(15):2384–98.
[21] Pataky GJ, Sehitoglu H, Maier HJ. High temperature fatigue crack growth of haynes 230. Mater Character 2013;75:69–78.
[22] Pataky GJ, Sangid MD, Sehitoglu H, Hamilton RF, Maier HJ, Sofronis P. Full field measurements of anisotropic stress intensity factor ranges in fatigue. Eng Fract Mech 2012;94:13–28.
[23] Rabbolini S, Pataky G, Sehitoglu H, Beretta S. Fatigue crack growth in haynes 230 single crystals: an analysis with digital image correlation. Fatigue Fract Eng Mater Struct 2015;38(5):583–96.
[24] Irwin GR. Plastic zone near a crack and fracture toughness. In: Proceedings of the 7th Sagamore ordinance materials research conference; 1960. p. 63–78.
[25] Gao H, Alagok N, Brown MW, Miller KJ. Growth of fatigue cracks under combined mode i and mode ii loads. Multiaxial fatigue: a symposium, vol. 853. ASTM International; 1985. p. 184.
[26] Rice J. The mechanics of crack tip deformation and extension by fatigue, fatigue crack propagation. ASTM, ASTM STP; 1966. p. 415.
[27] McClung R, Sehitoglu H. On the finite element analysis of fatigue crack closure1. Basic modeling issues. Eng Fract Mech 1989;33(2):237–52.
[28] McClung R, Sehitoglu H. On the finite element analysis of fatigue crack closure2. Numerical results. Eng Fract Mech 1989;33(2):253–72.
[29] Newman Jr JC. A finite element analysis of fatigue crack closure. ASTM STP 590; 1976. p. 281–301.

[30] Pommier S, Bompard P. Bauschinger effect of alloys and plasticity-induced crack closure: a finite element analysis. Fatigue Fract Eng Mater Struct 2000;23(2):129–40.

[31] Pommier S. Plane strain crack closure and cyclic hardening. Eng Fract Mech 2002;69(1):25–44.

[32] Roychowdhury S, Dodds RH. A numerical investigation of 3-d small-scale yielding fatigue crack growth. Eng Fract Mech 2003;70(17):2363–83.

[33] Healy B, Gullerud A, Koppenhoefer K, Roy A, Roy-Chowdhury S, Petti J, et al. Warp3d: 3-d dynamic nonlinear fracture analyses of solids using parallel computers, structural research series (srs 607) uilu-eng-95-2012, University of Illinois at Urbana-Champaign; 2015.

[34] Shah P, Tan C, Wang X. T-stress solutions for two-dimensional crack problems in anisotropic elasticity using the boundary element method. Fatigue Fract Eng Mater Struct 2006;29(5):343–56.

[35] Hertzberg R. Deformation and fracture mechanics of engineering materials. New York: John Wiley and sons; 2012.

[36] Hill R. The mathematical theory of plasticity, vol. 11. Oxford University Press; 1950.

[37] Lee EH. Elastic–plastic deformation at finite strains. J Appl Mech 1969;36 (1):1–6.

[38] Kocks W. Thermodynamics and kinetics of slip. Prog Mater Sci 1975;19:291.

[39] Kok S, Beaudoin A, Tortorelli D. A polycrystal plasticity model based on the mechanical threshold. Int J Plast 2002;18(5):715–41.

[40] Smith R, Miller K. Fatigue cracks at notches. Int J Mech Sci 1977;19(1):11–22.

[41] Beretta S, Rabbolini S, Di Bello A. Multi-scale crack closure measurements with digital image correlation on haynes 230. Fract Struct Integrity 2015 (33):174–82.

[42] Tada H, Paris P, Irwin G. The analysis of cracks handbook. New York: ASME Press; 2000.